



Article

Hydrogen Embrittlement Susceptibility of New Generation Advanced High-Strength Steels for Automotive Applications

James Lelliott ^{1,*} , Elizabeth Sackett ² , Neil McMurray ² and Douglas Figueroa-Gordon ¹ ¹ Tata Steel UK, Port Talbot, South Wales SA13 2NG, UK; d.figueroagordon@tatasteeleurope.com² School of Engineering and Applied Sciences, Swansea University, Swansea SA1 8EN, UK; e.sackett@swansea.ac.uk (E.S.)

* Correspondence: james.elliott@tatasteeleurope.com

Abstract

The adoption of advanced high-strength steels (AHSS) in the automotive industry has significantly increased in recent years driven by weight reduction and enhanced crash-worthiness. Hot dip galvanised sacrificial coatings are regularly applied to these steels for corrosion protection. In this investigation, the scanning vibrating electrode technique (SVET) demonstrated that hydrogen evolution on the steel substrate is taking place when these sacrificial coatings are damaged during service, increasing the risk of hydrogen embrittlement. The hydrogen embrittlement susceptibility of a new generation of nano-precipitate ferritic, FNP, AHSS have been studied and compared against conventional dual phase ferritic-martensitic, FM, AHSS at equivalent strength levels. Hydrogen permeation tests have shown that FNP AHSS have lower effective diffusion coefficients, D_{eff} , than FM AHSS at equivalent strength levels. At 800 MPa strength levels D_{eff} were $1.68 \times 10^{-7} \text{ cm}^2/\text{s}$ and $1.87 \times 10^{-7} \text{ cm}^2/\text{s}$ for FNP800 and FM800, respectively. At higher strength levels, 1000 MPa, D_{eff} were $7.45 \times 10^{-8} \text{ cm}^2/\text{s}$ and $1.45 \times 10^{-7} \text{ cm}^2/\text{s}$ for the FNP1000 and FM1000, respectively. Slow strain-rate tests (SSRT) showed that FNP AHSS displayed over 35% higher resistance to hydrogen embrittlement than conventional FM AHSS. Quantitative fractographic analyses confirmed that the new ferritic nano-precipitate microstructure retains much more ductile behaviour than conventional martensitic-ferritic even under the most severe hydrogen charging conditions tested.

Keywords: hydrogen embrittlement susceptibility; advanced high strength steels; automotive; nano precipitate ferritic steel; ferritic martensitic steel

Academic Editors: Marina Cabrini,
David M. Bastidas and Raman Singh

Received: 13 October 2025

Revised: 15 November 2025

Accepted: 21 November 2025

Published: 24 November 2025

Citation: Lelliott, J.; Sackett, E.; McMurray, N.; Figueroa-Gordon, D. Hydrogen Embrittlement Susceptibility of New Generation Advanced High-Strength Steels for Automotive Applications. *Corros. Mater. Degrad.* **2025**, *6*, 61. <https://doi.org/10.3390/cmd6040061>

Copyright: © 2025 by the authors. Licensee MDPI, Basel, Switzerland. This article is an open access article distributed under the terms and conditions of the Creative Commons Attribution (CC BY) license (<https://creativecommons.org/licenses/by/4.0/>).

1. Introduction

The use of advanced high-strength steels (AHSS) in vehicle structures, chassis, and suspension components have significantly increased in recent decades from an average 2% to >15%, driven by enhanced manufacturability, crashworthiness, and weight reduction potential. Typical automotive components manufactured with AHSS include A-pillars, B-pillars, floor and roof cross members, front and back crush box, battery packages, suspensions arms, and many others [1–4].

Conventional Dual-Phase AHSS is widely used in safety cage components, outer body, and floor panels [5]. Its microstructure comprises an array of second-phase martensite embedded in a ferrite matrix with strength levels typically increasing up to 1000 MPa, as martensite and bainite volume fraction increases [6,7]. The presence of ferrite and

martensite improves the work-hardening characteristics as strain is concentrated in the softer ferrite phase, increasing resistance to localised thinning [7].

In more recent years, a new generation of AHSS has been developed with improved hole expansion and fracture toughness characteristics. These new AHSSs have a fine-grained microstructure with nominally 100% ferrite. Within this ferrite matrix are inter-phase precipitated (IP) carbides and carbonitrides of Nb, Ti, V, and Mo. Whilst some of these micro-alloy precipitates promote grain refinement, a substantial amount of strength from precipitation strengthening is gained from these carbonitrides [8,9]. As the micro-alloy elements are typically added in quantities that are stoichiometric (or greater), they combine fully with the available carbon to ensure the microstructure contains virtually no Fe_3C . The absence of hard second phases (martensite, bainite, Fe_3C) inhibits void nucleation and suppresses fracture during loading, offering an advantage of greatly improved stretch-flangeability over multi-phase AHSS [10,11].

Sacrificial galvanic coatings are commonly applied to these steel components to protect them from rust and corrosion. Zn-based galvanised coatings are the most accepted in the automotive industry [12]. However, should these coatings become damaged during service, a galvanic cell could be generated in the presence of an electrolyte such as salty water, as depicted in Figure 1. Whilst anodic reactions arise in the sacrificial zinc coating (Equation (1)) the steel substrate becomes the cathode where hydrogen evolution takes place (Equation (2)). Other cathodic reactions could take place (Equations (3) and (4)), depending on local pH levels.

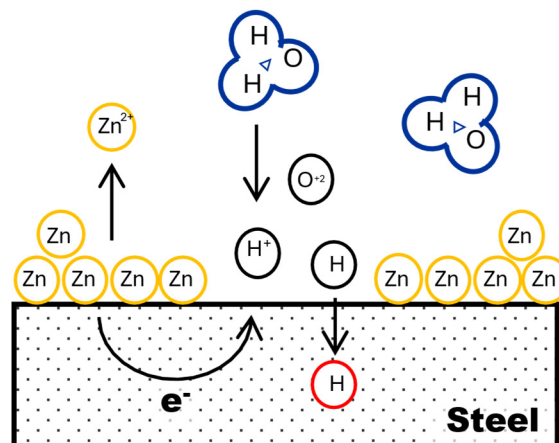
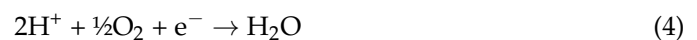
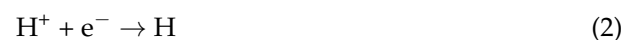
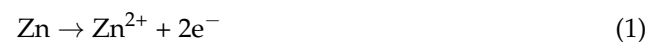


Figure 1. Schematic representation of hydrogen embrittlement of steels due to corrosion of a zinc sacrificial coating.

At the cathodic surface atomic hydrogen can be absorbed directly beneath the steel substrate following the coupled discharge-recombination mechanism [13,14]. Over time hydrogen diffuses within the steel microstructure in sufficient quantities, increasing the risk to hydrogen embrittlement (HE) and its associated deterioration of mechanical properties.

Automotive steel grades considered in the present study are also regularly used in the galvanised condition, and it is therefore important to understand how hydrogen evolution and uptake take place when the sacrificial coating becomes damaged in service. The

Scanning Vibrating Electrode Technique, SVET, has been shown to be an effective technique to quantify galvanic corrosion on hot-dipped galvanised steels [15,16].

Ingress of atomic hydrogen into the steel greatly lowers its strength, ductility, and toughness, causing it to fail under loads well below those expected during service. Proposed HE mechanisms for steels are either based on lattice decohesion, where diffusing hydrogen weakens lattice bonds, or hydrogen-induced plasticity, where diffusing hydrogen reduces the stress required for formation and motion of crystal imperfections associated with plastic deformation, such as dislocations [17–19]. It is also recognised that hydrogen embrittlement susceptibility increases with strength levels. Nonetheless, hydrogen diffusivity within the steel microstructure plays a key role [20]. In the present study, the hydrogen embrittlement susceptibility of the latest generation ferritic nano-precipitate (FNP) is compared to that of more conventional dual-phase ferritic-martensitic (FM) AHSS at equivalent strength levels via use of slow strain-rate (tensile) tests (SSRT), with hydrogen diffusion coefficients measured using the well-established potentiostatic permeation technique [21].

2. Materials and Methods

2.1. Materials

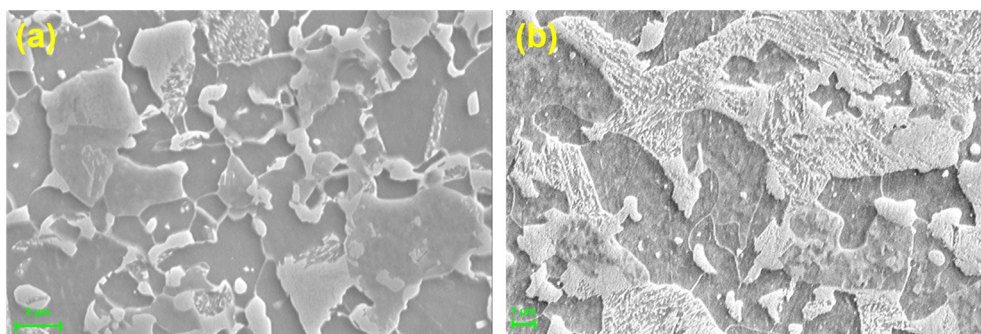
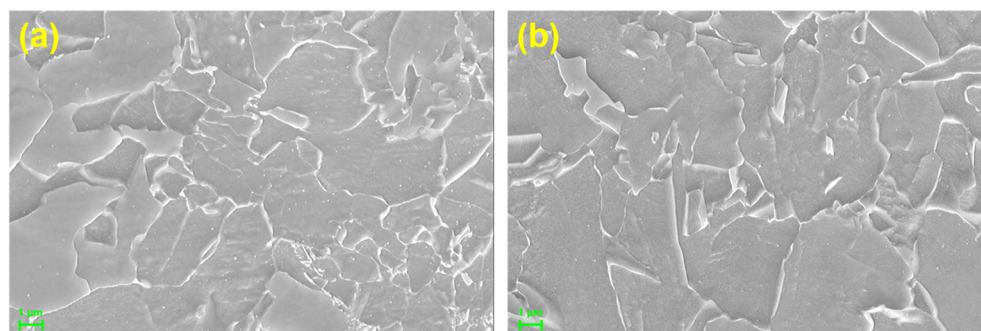
AHSS considered in the current work include conventional ferrite-martensite dual-phase steels with strength levels of 800 and 1000 MPa, identified as FM800 and FM1000. The new generation ferritic nanoprecipitate AHSS at equivalent strength levels were identified as FNP800 and FNP1000, respectively. Chemical compositions for these steels are displayed in Table 1, with baseline mechanical properties assessed via conventional tensile tests shown in Table 2. Microstructural characterisation was carried out using a Zeiss Evo scanning electron microscope (Carl Zeiss Industrielle Messtechnik GmbH, Oberkochen, Germany) operating at 20 kV accelerating voltage, 100–150 pA probe current. Grain size analysis was performed via the linear intercept method using Matlab (R2019b) software [6,22]. The typical microstructure of the FM steels can be seen in Figure 2, with the darker regions showing the ferrite (α) phase, and the lighter regions the martensite (α') phase. Relative volume fractions of each phase were estimated using segmentation technique in ImageJ (1.52q) software [23]. Martensite volume fractions were 40% and 55% for FM800 and FM1000, respectively. These values were comparable with the figures obtained from the literature [24,25]. The FNP steels appear to have a 100% ferrite microstructure and an average grain size of 2.3 μm (diameter). There is little evidence of any Fe_3C formations, either lamellar or globular, as shown in Figure 3.

Table 1. Alloy chemistry for the steels studied in this work (figures in mass-percent).

Steel	C	Si	Mn	Cr	Mo	Nb	Ti	V	B
FM800	0.136	0.236	1.692	0.553	0.003	0.024	0.021	0.003	0.0002
FNP800	0.0611	0.189	1.373	0.016	0.141	0.061	0.002	0.212	0.0002
FM1000	0.149	0.041	2.222	0.548	0.005	0.014	0.026	0.006	0.0001
FNP1000	0.1037	0.201	1.396	0.023	0.292	0.05	0.003	0.286	0.0002

Table 2. Baseline average mechanical properties of the studied steels.

Product	$R_{p0.2}$ [MPa]	R_m [MPa]	A_g [%]	A_{50} [%]
FM800	488 (± 2)	782 (± 4)	12.5 (± 0.1)	19.7 (± 0.3)
FNP800	747 (± 12)	826 (± 5)	9.3 (± 0.3)	17.2 (± 1.5)
FM1000	700 (± 5)	1027 (± 9)	7.8 (± 0.3)	13.5 (± 0.4)
FNP1000	862 (± 8)	982 (± 3)	8.2 (± 0.1)	16.7 (± 0.3)

**Figure 2.** SEM micrographs of (a) FM800; (b) FM1000, at 5000 \times magnification.**Figure 3.** SEM micrographs of (a) FNP800; (b) FNP1000, at 5000 \times magnification.

2.2. Effect of Galvanic Corrosion upon Hydrogen Evolution

To examine the impact of galvanic corrosion on hydrogen evolution, the local anodic and cathodic current densities during immersion in 0.1 M NaCl solutions were quantified using a scanning vibrating electrode technique (SVET). One half of the surface of a 30 \times 30 mm zinc-coated coupon was ground with P1200-grit silicon carbide grinding paper to expose the steel substrate (using ethanol as lubricant to avoid inducing corrosion prior to immersion). SVET measurements were undertaken using a probe tip 250 μ m in diameter, mounted on a moving coil electromagnetic driver connected to a 140 Hz vibrating probe [15,16,26]. Figure 4 shows a schematic of the SVET tip and housing. Scans were undertaken every 30 min over the course of 24 h to provide a series of spatial and time-resolved current density measurements along the axis of measurement, J_z , across the surface. Data post-processing was performed using Golden Surfer 10 (10.7.972) and Matlab software.

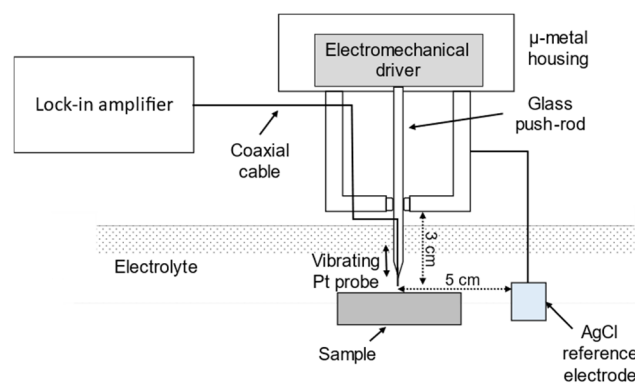


Figure 4. Schematics of the scanning vibrating electrode technique, SVET (adapted from [15]).

2.3. Hydrogen Diffusion

Hydrogen diffusion coefficients were measured using a Devanathan–Stachurski cell [21] as depicted schematically in Figure 5.

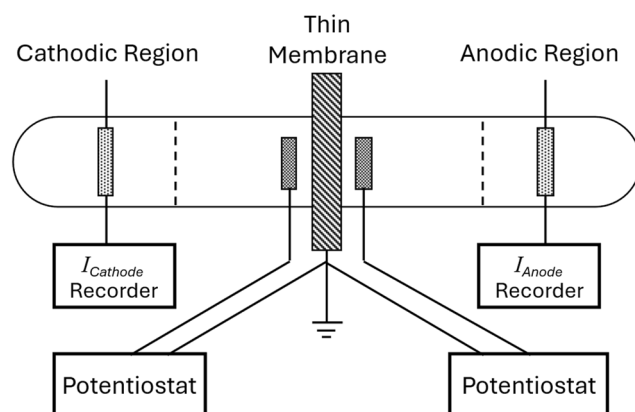


Figure 5. Schematic of Devanathan–Stachurski permeation cell setup.

Permeation samples had nominal thickness of 0.8 mm with charging surface area of 2.011 cm². The charging cell contained a 3.5% NaCl + 3 g/L NH₄SCN, pH 4.56, while the oxidation cell contained 0.1 M NaOH solution, pH 13. A charging potential of −1050 mV vs. saturated calomel electrode (SCE) was applied after preliminary desorption cycles were completed, typically after 14 h. As diffusing hydrogen is oxidised it generates a corresponding measurable current until it reaches steady state, generating a characteristic permeation curve. The current I_t , at time t , is converted to a hydrogen permeation flux, J_t , with the following equation [27]:

$$J_t = (I_t / A) / F \quad (5)$$

where A is the surface area exposed to the electrolyte in the oxidation cell, and F is the Faraday constant (96,485 coulombs/mol). The lag time, t_{lag} , described as the time taken when $J_t / J_\infty = 0.63$, was used to calculate the effective diffusion coefficient, D_{eff} , according to the following equation:

$$D_{eff} = L^2 / (6t_{lag}) \quad (6)$$

where L is the membrane thickness in cm. The surface concentration of hydrogen at the charging side was calculated according to the following equation:

$$C_0 = (J_\infty L) / D \quad (7)$$

The values obtained for these parameters from the experimental data, along with membrane thickness, were then input to a bespoke Matlab script [1] used to simulate the

perfect ‘Fickian’ curve for a given sample as a comparison to the curve obtained from the experimental data. For potentiostatic charging the transient of the permeation flux according to Fick’s diffusion laws is recreated by the following equation:

$$J_t = \frac{D_{eff}C_0}{L} \left\{ 1 + 2 \sum_{n=1}^{\infty} \cos(\pi n) \text{Exp} \left(\frac{-Dn^2\pi^2 t}{L^2} \right) \right\} \quad (8)$$

2.4. Embrittlement Indices, EI, and Slow Strain-Rate Test, SSRT

For its relative simplicity and reproducibility [28] mechanical property degradation due to hydrogen was assessed using slow strain-rate tensile tests, SSRT. Sample nominal thickness was 0.8 mm and the total length 64 mm. SSRTs were carried out at a nominal strain rate of 8.33×10^{-6} /s. This strain rate is around 10,000 times slower than that used in standard tensile tests on production material (e.g., [29]) and is of an order that is fairly typical of SSRT which is widely used in studying the deleterious effects of hydrogen on mechanical properties [28]. The slow strain rate is essential in allowing sufficient opportunity for hydrogen to diffuse to all parts of a sample, accumulating and interacting with regions of high stress or microstructural imperfections [30–33]. Tests at higher strain rates raise the chances of fracture occurring only at regions directly adjacent to the charging medium [34], raising the possibility that key microstructural differences may be overlooked. Furthermore, dislocation motion itself can act as a hydrogen transport mechanism, necessitating strain rates as low as practicable [35]. For SSRT involving hydrogen charging in this work, a bespoke cell was placed around the sample gauge length with approximately 30 mL of 3.5% NaCl + 3 g/L NH_4SCN . Samples were potentiostatically polarised at -1050 mV versus a saturated calomel reference electrode, SCE, with a platinum foil counter electrode. After loading the sample and charging apparatus to the tensile test machine (Instron 8516 (Instron, Norwood, MA, USA)) hydrogen charging was undertaken in situ for 2 h prior to straining and was maintained throughout the duration of the test. The hydrogen embrittlement index, EI, was assessed according to the decrease in time to failure, TTF, calculated according to the following equation:

$$\text{Embrittlement Index} = (\text{Time to failure in air} - \text{Time to failure in hydrogen}) / \text{Time to failure in air} \quad (9)$$

Student’s *t*-test was used to determine whether there were statistically significant differences between test populations. Comparing the means of the two data populations enables calculation of a test statistic, *t*, through the equation:

$$t = ((m_1 - m_2)) / (s \sqrt{((1/n_1 + 1/n_2)))} \quad (10)$$

where m_1 and m_2 represent the means of the two data sets, and n_1 and n_2 the number of measurements in each set. *s* is calculated from the standard deviations of the two populations:

$$s^2 = (s_1^2 + s_2^2) / 2 \quad (11)$$

where s_1 and s_2 represent the standard deviations of the two data sets. The test statistic, *t*, is then compared with tabulated values for a 95% confidence level with $((n_1 - 1) + (n_2 - 1))$ degrees of freedom. If the test statistic < *t*-distribution, with a 95% confidence level the datasets belong to the same population, i.e., acceptance of the null hypothesis [36].

Weibull distributions were used to show the probability of survival of a group of specimens before failure through hydrogen embrittlement. The time-to-failure data for each set of product–test condition pairs was compared with a mean time to failure of the uncharged condition for each of the steels. The Weibull model was adapted for analysis

through brittle failure, in showing that the probability of a specimen not failing within a specified time, t , is calculated according to the following equation [36]:

$$P_{(s)} = 1 - P_{(f)} = e^{-xt} \quad (12)$$

where $P_{(s)}$ is the probability of survival, $P_{(f)}$ the probability of failure, and x the shape parameter known as the Weibull slope. x is the probability per unit time, t , that a crack forms of sufficient severity to cause failure of the specimen and is deduced from the negative gradient of a plot of $\ln P_{(s)}$ versus t . As there is a minimum time for a critical crack to initiate, t_i , the graph is displaced along the time axis by this amount, i.e., when $P_{(s)} = 1$, $\ln P_{(s)} = 0$, and $t = t_i$, modifying Equation (12) to become [37]:

$$P_{(s)} = 1 - P_{(f)} = e^{-x(t-t_i)} \quad (13)$$

2.5. Fractography

Fracture surface analysis was undertaken by SEM across the entire fracture surfaces of selected samples ($1 \times$ “dry” specimen per steel, $2 \times$ hydrogen-charged specimens per steel). Images were then stitched and analysed using ImageJ software. Regions of the fracture surface were assigned a colour depending on the dominant features observed in a particular location. Quasi-cleavage (QC) facets and regions of intergranular (IG) fracture represented a more brittle fracture mode, whereas micro void coalescence (MVC), shear voids, and tear ridges (TR) occurred in more ductile failures. Trans-granular (TG) cracks can be found in both ductile and brittle regions, and typically occur where both mechanisms are present, as shown in Figure 6. Fractographic quantitative assessment was carried out using Matlab software to count the pixels from each assigned colour for each fractograph and summarise as percentages.

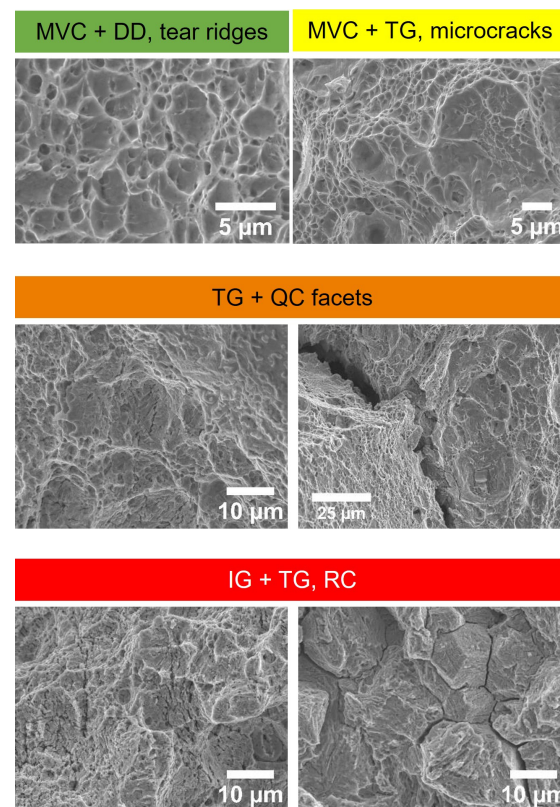


Figure 6. Examples illustrating how different fracture surface features were classified for quantitative analysis.

3. Results and Discussion

3.1. Galvanic Corrosion and Hydrogen Evolution

Figure 7 shows a selection of contour plots of SVET scan data displaying regions of cathodic (blue) and anodic (red) activity as galvanic corrosion process in the relatively weak 0.1 M NaCl solution. Regions with relatively high localised anodic activity, current density up to 6.01 A/m^2 , take place as the Zn sacrificial coating is corroded in a localised manner. At the exposed steel substrate a wide region with cathodic current densities (blue) is shown with a maximum cathodic current density of -0.53 A/m^2 . This current density is indicative of cathodic polarisation at the steel surface that promotes hydrogen evolution, albeit in competition with a diffusion-limited oxygen reduction reaction [38]. After 2.5 h, the anodic regions (red) begin to expand, but with lower intensity, indicating that localised pitting has ceased and corrosion of the zinc has become more general. The cathodic regions periodically develop some localised regions of increased cathodic current density, particularly after about 14 h, peaking around 20 h. After 24 h, both anodic and cathodic activity had reduced intensity from peak current densities in these localised, previously high-intensity regions. Figure 8 shows the averaged anodic and cathodic current densities, I_a and I_c , respectively, calculated according to Equation (14) (the equivalent for anodic current density with respect to time, J_{at} , calculated using $J_z(x,y) > 0$).

$$I_c = A \cdot J_{ct} \geq \int_0^y \int_0^x [J_z(x,y) < 0] dx dy \quad (14)$$

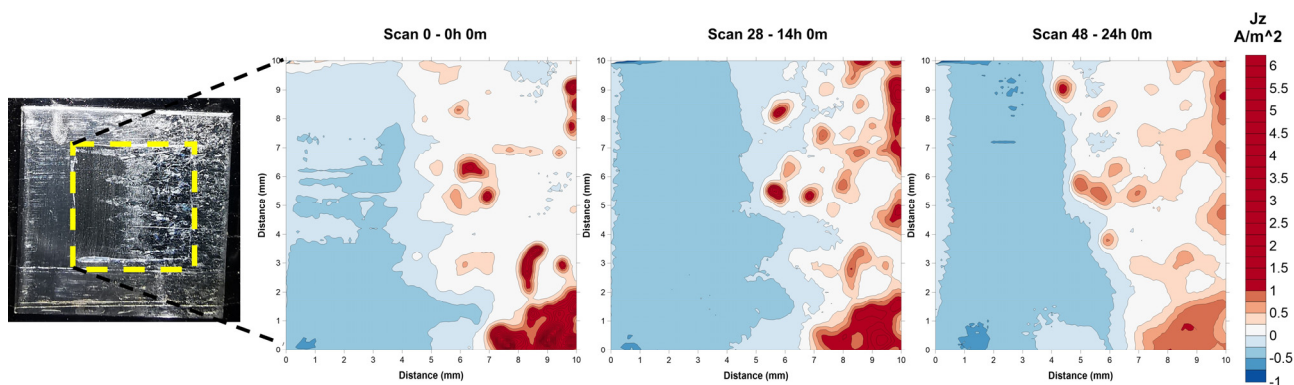


Figure 7. SVET contour plot of a galvanised steel sample with coating partially damaged to expose the steel substrate, with the corresponding optical image. Contour plot shows scan taken at time = 0, 14, and 24 h immersion in 0.1 M NaCl solutions. Contour lines displayed every $\pm 0.25 \text{ A/m}^2$ current density.

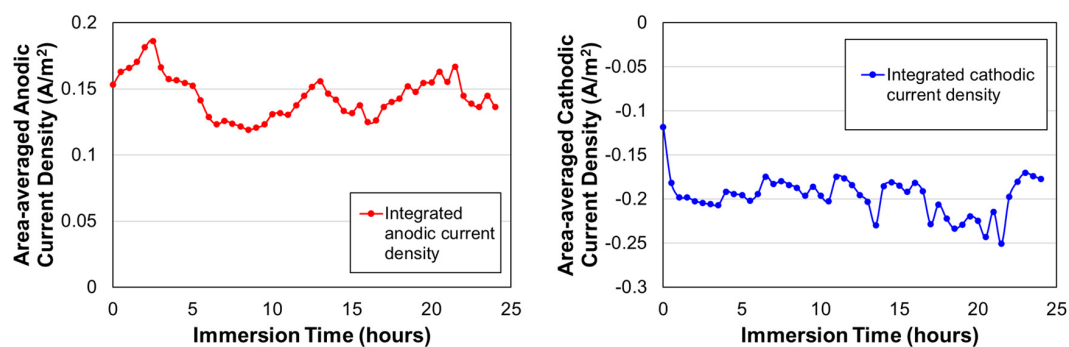


Figure 8. The area-averaged anodic and cathodic current densities, I_a and I_c , respectively. (Left)—area-averaged anodic current density over 24 h; (Right)—area-averaged cathodic current density over 24 h.

The measured total anodic current density shows greater stability over the 24 h duration of the test than the maximum current density plot, indicating there is significant sacrificial corrosion of the zinc coating as the immediate pitting behaviour subsides and continues throughout. Cathodic current density measurements show a degree of fluctuation but measure consistently higher than the anodic current density, as illustrated in Figure 8. The most strongly cathodic areas showed current density below -0.3 A/m^2 , of a similar order to cathodic current densities seen during potentiostatic hydrogen charging (at -1050 mV SCE in 3.5% NaCl) for both permeation and slow strain-rate tests. By applying Faraday's Law, it is possible to calculate an estimate for the total hydrogen evolved at the exposed steel surface according to equation:

$$Q = \int_{t=0}^{t=t_m} J_{ct} \cdot dt \quad (15)$$

where Q is the total charge in C/m^2 and t_m the scan time in seconds, with integration performed numerically and assuming that J_{ct} is constant between scans. Figure 9 shows calculated values for hydrogen evolved at the exposed steel surface over the duration of the experiment. The total hydrogen evolved over 24 h was $>1.6 \times 10^{-6} \text{ mols.H}$.

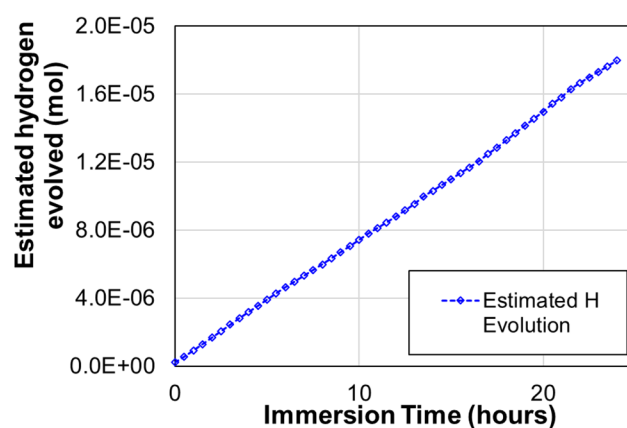


Figure 9. Estimated hydrogen evolution over the duration of the experiment.

3.2. Hydrogen Diffusion

Permeation curves for FM800 and FNP800 AHSS are shown in Figure 10. For FM800 the breakthrough time, t_b , was 1033 s, the lag time, t_{lag} , was 4397 s, and the maximum flux, J_∞ , was $2.2 \times 10^{-11} \text{ mol/cm}^2/\text{s}$. The calculated mean effective diffusion coefficient, D_{eff} , was $1.87 \times 10^{-7} \text{ cm}^2/\text{s}$, and the maximum hydrogen concentration at the charging surface, C_0 , was $8.51 \times 10^{-6} \text{ mol/cm}^2$. The FNP800 steel showed a t_b value of 3373 s, a t_{lag} of 6682 s, and J_∞ of $1.68 \times 10^{-11} \text{ mol/cm}^2/\text{s}$. The calculated mean effective diffusion coefficient, D_{eff} , was $1.68 \times 10^{-7} \text{ cm}^2/\text{s}$, and the maximum hydrogen concentration at the charging surface, C_0 , was $8.21 \times 10^{-6} \text{ mol/cm}^2$.

For AHSS at 1000 MPa strength, permeation curves in Figure 11 show that the FM1000 steel had t_b of 1481 s, a t_{lag} of 5445 s, and a J_∞ of $1.93 \times 10^{-11} \text{ mol/cm}^2/\text{s}$. The calculated mean effective diffusion coefficient, D_{eff} , was $1.45 \times 10^{-7} \text{ cm}^2/\text{s}$, and the maximum hydrogen concentration at the charging surface, C_0 , was $9.14 \times 10^{-6} \text{ mol/cm}^2$. The FNP1000 AHSS had t_b of 6628 s, a t_{lag} of 13,944 s, J_∞ of $1.20 \times 10^{-11} \text{ mol/cm}^2/\text{s}$, D_{eff} of $7.45 \times 10^{-8} \text{ cm}^2/\text{s}$, and C_0 of $1.54 \times 10^{-5} \text{ mol/cm}^2$. Figure 12 shows the differences between effective diffusion coefficient calculated from data obtained in permeation tests.

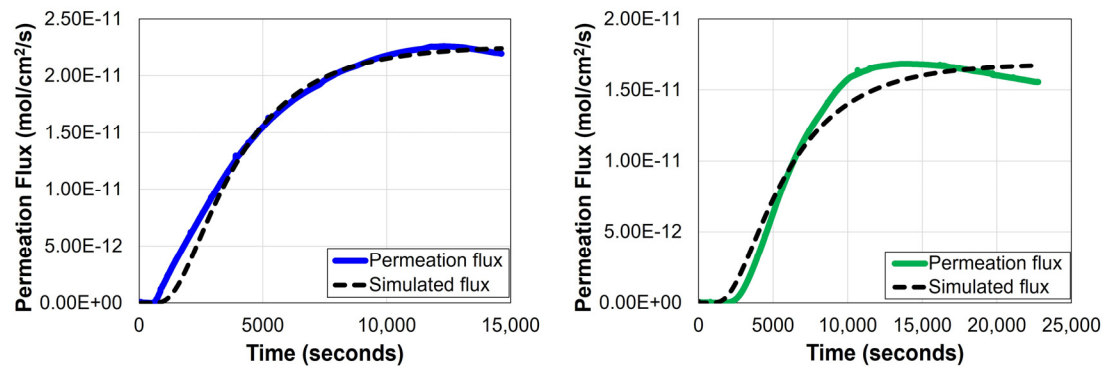


Figure 10. Hydrogen permeation flux (solid line) for (left)—FM800—and (right)—FNP800—membranes with 0.8 mm nominal thickness, charged at -1050 mV (SCE) in 3.5% NaCl + 3 g/L NH_4SCN .

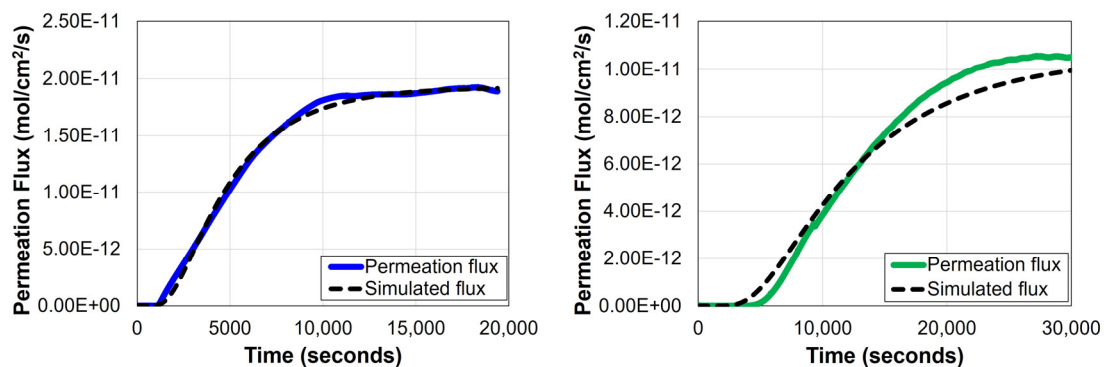


Figure 11. Hydrogen permeation flux (solid line) for (left)—FM1000—and (right)—FNP1000—membranes with 0.8 mm nominal thickness, charged at -1050 mV (SCE) in 3.5% NaCl + 3 g/L NH_4SCN .

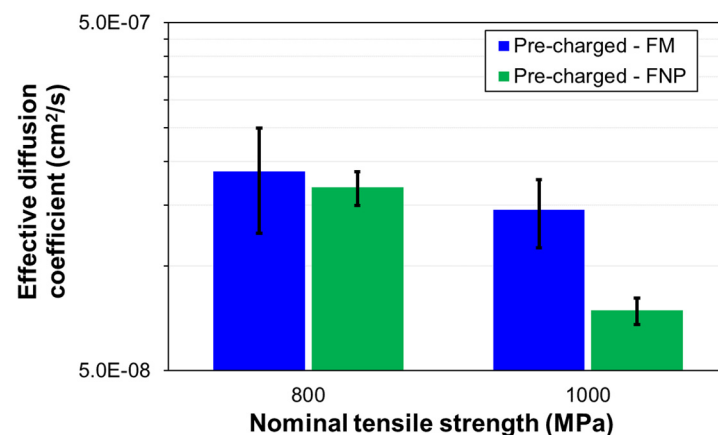


Figure 12. Calculated effective diffusion coefficient, D_{eff} , compared to nominal tensile strength for the different microstructures.

The fully ferritic FNP steels have shown to have much lower effective diffusivities than the equivalent ferrite-martensite FM steels at same strength levels. FNP steels exhibit clear differences between the permeation curves simulated according to Fick's laws and the measured permeation flux, as shown in Figures 10 and 11. The initial rising transient is displaced to a longer (delayed) breakthrough time, t_b , before rising more steeply than the simulated Fick's curves. This increase in t_b has been previously reported to be caused by a higher overall hydrogen trap density [39,40]. Permeation curves for FM steels at equivalent strength levels did not show a delay in t_b , indicating that the FNP steels contain a greater trap density than the equivalent strength FM steels.

As diffusible hydrogen saturates the irreversible traps before filling reversible traps or diffusing through the lattice, the overall hydrogen diffusivity is impacted to a greater degree by the presence of irreversible traps compared to reversible ones [41]. The overall shape of the permeation curve between t_b and J_∞ , however, is unlikely to be influenced by the presence of strong traps [42]. FNP steels might contain a relatively high density of irreversible trap sites, not necessarily high densities of reversible trap sites.

FNP steels are alloyed with Nb, V, and Mo resulting in the formation of nano precipitates including NbV, NbVMo, and carbide/carbo-nitride. It has been reported that such precipitates could act as irreversible traps, particularly if precipitates are very fine [17]. Depover [43–45] showed that Ti, V, Mo carbides are able to trap a significant amount of hydrogen in steels containing 0.1–0.3 wt.% C [46], and direct observation of hydrogen (in the form of deuterium) trapped at microalloy carbide nanoprecipitates has been reported by Takahashi (via gas charging) [47] and Chen (via electrolytic charging) [48]. Whilst grain refinement has been shown to increase hydrogen trapping through increase in grain boundary area [49], the lower relative diffusivity of the FNP steels and shape of the permeation transients suggest a much larger impact of the presence of nanoprecipitates in the microstructure. The lower relative diffusivity of the FNP steels could be associated with the presence of these nanoprecipitates in the microstructure.

FM steels with shallower permeation transients indicate the presence of low irreversible trap densities and higher density of reversible traps, more clearly illustrated in “normalised” permeation curves seen in Figure 13. FM steels contain substantial volume fractions of martensite, formed via a displacive transformation, resulting in high dislocation densities. Numerous studies have shown that dislocations represent reversible hydrogen traps, decreasing the gradient of the rising transient, but not impacting the overall effective diffusivity, D_{eff} , to the same degree as irreversible traps [50–53].

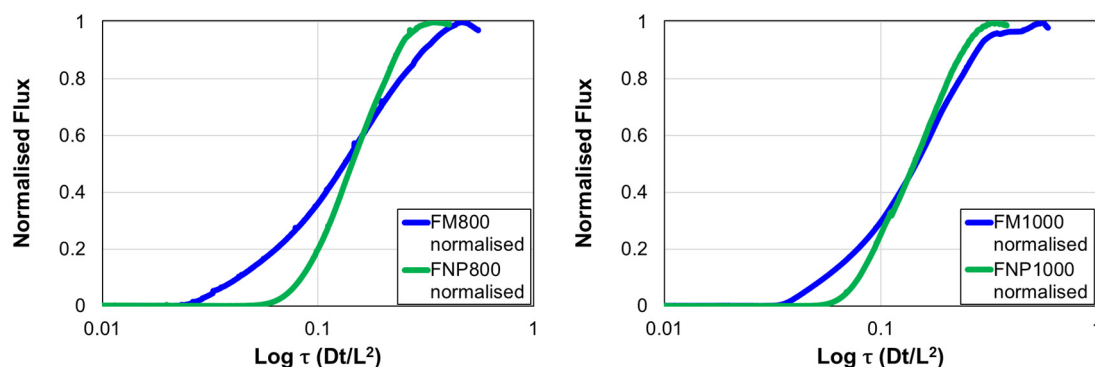


Figure 13. (Left): normalised hydrogen permeation curves for 800 MPa strength steels; (Right): normalised hydrogen permeation curves for 1000 MPa strength steels.

3.3. Slow Strain-Rate Tests and Fractography

Engineering stress and strain (or in this case percent elongation) are the standard measures by which mechanical properties for automotive steels are specified and the parameters against which they are tested. Without the use of extensometry (particularly reduction-in-width) due to the presence of the hydrogen charging apparatus it was not possible to calculate the instantaneous cross-sectional area of the sample during the test, required to calculate true stress.

A considerable reduction in ductility for FM800 steel due to hydrogen charging can be seen in Figure 14. The mean total elongation dropped from 18.9%, in the dry condition, to 9.4% in the hydrogen-charged condition. The mean TTF value for the dry condition was 6.3 h, reducing to 3.1 h for the dry and hydrogen-charged condition, respectively. Weibull plots in Figure 15 showed that TTF values were consistent for each test condition. Student’s

t -test results showed with a 95% confidence that there is a statistically significant difference between the two populations, dry and hydrogen-charged conditions.

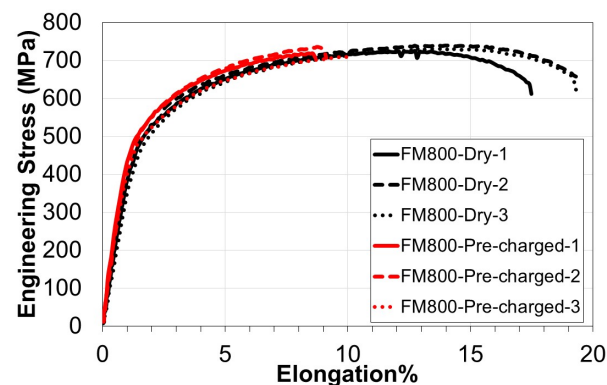


Figure 14. Engineering stress-elongation curves for slow strain-rate tests for FM800 under each condition.

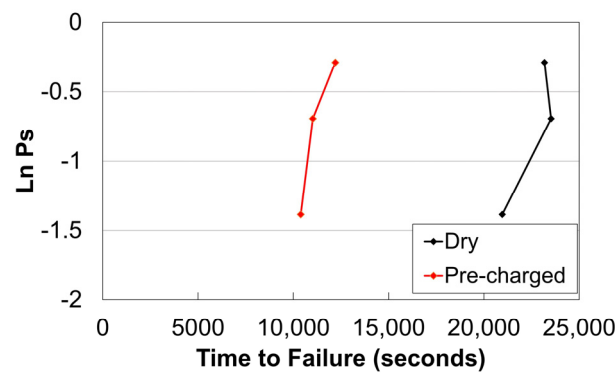


Figure 15. Simplified Weibull plots for FM800 slow strain-rate tests, showing differences in ‘survival’ times for the test specimens. Changes in gradient reflect the range of times that an FM800 specimen could be expected to ‘survive’ under the specified test conditions.

Figure 16 shows FNP800 mean total elongation dropped from 18.9%, in the dry condition to 12.8%, in the hydrogen pre-charged condition, although one of the tests (pre-charged test 3) appears to have persisted to a significantly higher elongation than the others for the same conditions. It could be argued that the reduction in ductility during the pre-charged tests on FNP800 is within the scatter of the dry test condition, showing substantially less obvious reduction in elongation than for the equivalent strength FM steel. Student’s t -test results showed with a 95% confidence that there was no statistically significant difference between the conditions tested, although the Weibull suggests two distinct populations when compared according to TTF.

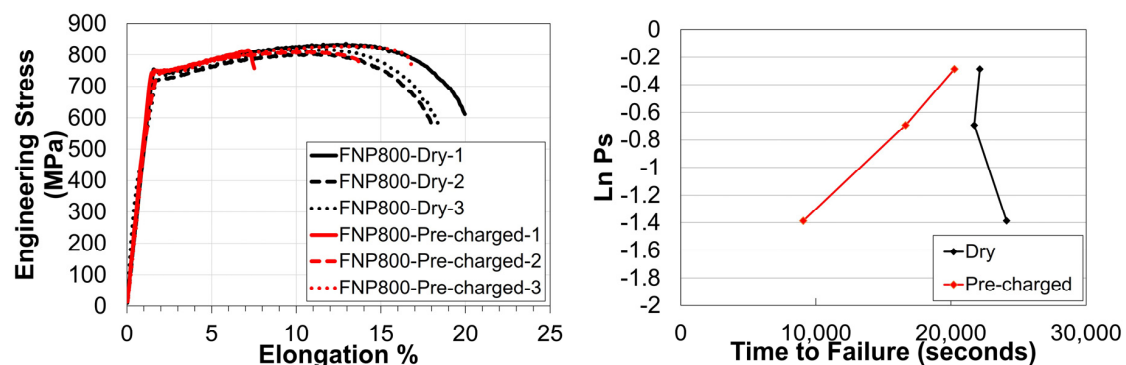


Figure 16. (Left): SSRT stress-elongation curves for FNP800 for the different charging conditions; (Right): simplified Weibull plots showing differences in survival times for FNP800.

SSRT curves for FM1000 are shown in Figure 17. A severe loss of ductility is shown for the hydrogen charged condition, with mean total elongation dropping from 18.5%, in dry tests, to just 4.6% for hydrogen charged tests. The mean TTF was reduced from 22,158 s to 5418 s. FM1000 experienced a large drop in performance in the presence of hydrogen, and this is validated in the output of the *t*-tests. FNP1000 SSRT curves are shown in Figure 18. The mean total elongation was reduced from 17.4% to 10.0%, for the dry and hydrogen-charged conditions, respectively. TTF mean values decreased from 20,762 s in the dry condition to 11,633 s for the hydrogen-charged condition.

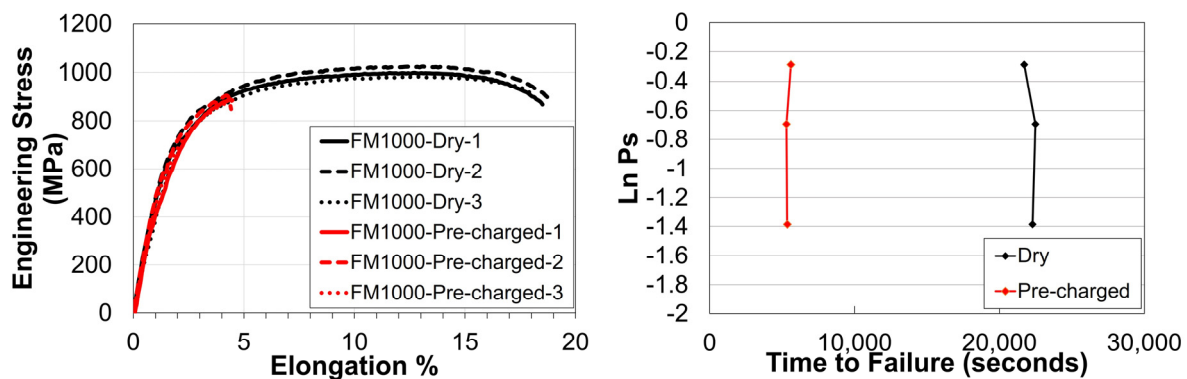


Figure 17. (Left): SSRT stress-elongation curves for FM1000 for the different charging conditions; (Right): simplified Weibull plots showing differences in survival times for FM1000.

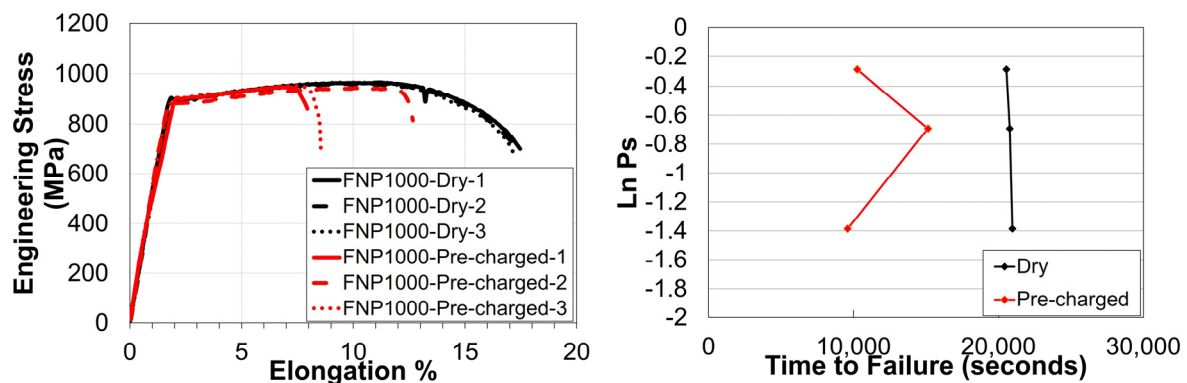
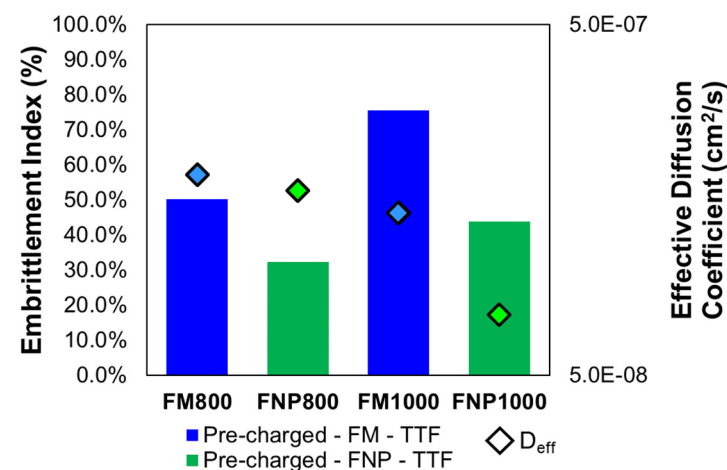


Figure 18. (Left): SSRT stress-elongation curves for FNP1000 for the different charging conditions; (Right): simplified Weibull plots showing differences in survival times for FNP1000.

Embrittlement indices for all AHSSs considered are summarised in Table 3. It is clear that at a given strength level, the fully ferritic FNP AHSS showed significantly lower hydrogen embrittlement susceptibility than the conventional ferritic-martensitic FM AHSS. It is notable that within strength levels this shows a clearer correlation with the relative effective diffusivity as shown in Figure 19. Differences in hydrogen embrittlement susceptibility between FNP and FM steels at equivalent strength levels are due to the distinctive microstructures.

Table 3. Mean embrittlement indices and output from Student's *t*-test for SSRTs. All *t*-tests based on time-to-failure in the pre-charged versus dry conditions.









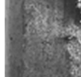




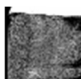



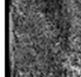
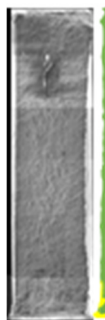



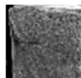

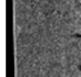

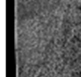




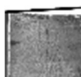

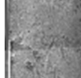

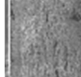
Product	Mean Embrittlement Index %	t-Statistic	p-Value	Power
FM800	50.30% ($\pm 3.5\%$)	11.773	2.98×10^{-4}	1
FNP800	32.40% ($\pm 16.7\%$)	2.168	0.096	0.38
FM1000	75.60% ($\pm 0.6\%$)	66.706	3.03×10^{-7}	1
FNP1000	43.80% ($\pm 11.5\%$)	5.186	6.58×10^{-3}	0.97

**Figure 19.** Embrittlement indices (bars, left y-axis) with overlaid effective diffusion coefficients (diamonds, right y-axis) of the steels in this study.

Several studies on dual-phase steels have shown that the ferrite-martensite microstructure may be inherently susceptible to hydrogen embrittlement. Koyama [54] found that hydrogen charging facilitates the nucleation of cracks in the martensite phase by decreasing the critical strain required for such an initiation (via the mechanism known as hydrogen-enhanced decohesion (HEDE)), promoting cracking at the ferrite/martensite boundaries, and trans-granular failure. Takashima [55] also found that where stress is sufficiently high, cracks will propagate through the martensite, avoiding the ferrite phase and causing a unique fracture surface with irregular roughness. Trans-granular cracking in the ferrite phase and cracking at ferrite/martensite boundaries are mechanisms more commonly associated with hydrogen-enhanced localised plasticity (HELP).

Evidence for these mechanisms in the FM AHSS can be found in the fractographic analysis. Fracture surface features, categorised and assigned colours according to the logic described in Figure 6, are summarised in Table 4. For all specimens tested in the dry condition, virtually the entire surface shows the presence of micro-void coalescence (MVC), considered to be typical of plastic deformation. In contrast, regions with the highest hydrogen concentrations closest to the charging surfaces possess widespread quasi-cleavage (QC) and intergranular cracking (IG), both indicative of a decohesion initiation and propagation. Regions further from the charging surfaces there is still the presence of (MVC), but with widespread trans-granular (TG) cracks.

Table 4. Surface feature classification within fractured SSRT specimens.

	Dry Condition		Hydrogen-Charged Condition	
FM800				100%
				0%
				79%
				4%
FNP800				100%
				0%
				0%
				17%
FM1000				100%
				11%
				53%
				15%
FNP1000				100%
				0%
				21%
				0%

Brittle fracture features are more prevalent in the FM steel than the FNP steels of equivalent strength levels, with increased visible damage near the charging surfaces. There is a greater prevalence of visible damage towards the specimen centres and comparatively more widespread transverse cracks, contributing to FM1000 showing nearly 100% prevalence of brittle features. In the most severely embrittled FM1000, QC facets are still apparent even at the very centre of the specimen. However, the presence of TG cracks and MVC in regions also containing QC might suggest that hydrogen may be lowering the critical stress for dislocation motion, proposed in the HELP mechanism [54].

Mixed modes of fracture are also observed in the single-phase FNP steels, but not to the extent observed in the FM steels. With EI of 32% and 44% for FNP800 and FNP1000, respectively, typically brittle fracture features covered up to 36% and 46%, respectively. However, only at the regions adjacent to the charging surfaces where hydrogen concentrations are at a maximum, are features such as QC and IG prevalent, in stark contrast to the equivalent FM specimens. Differences in embrittlement index and fracture features observed between FNPs and FMs steels are a clear indication of the inherently better performance of the FNP microstructure in presence of hydrogen. The microalloy precipitates and their interface with the ferrite matrix in FNP steels lowers the hydrogen available to cause damage via trapping and virtually eliminates the presence of hard second phases and associated interfaces where damage initiation could occur. Furthermore, precipitation strengthening inhibits dislocation motion, assisting in stressing the HELP mechanism [56]. Conversely, with a continuous supply of hydrogen these very hard nanoprecipitates may themselves act as crack initiation sites as the local hydrogen concentration and stress concentration exceed critical thresholds [57,58]. In the FM microstructure hydrogen trapping occurs primarily due to dislocations present in high density within the martensite phase. This presents FM steels with two problems: firstly, during pre-charging the hydrogen uptake is at its highest within the martensite phase providing high local hydrogen concentrations at potential crack initiation sites [54,59]; secondly, at the onset of deformation strain is concentrated in the ferrite phase, which then begins to occlude greater concentrations of hydrogen as dislocation density rises, rendering it less effective at arresting cracks that may initiate in the martensite phase [54,55].

Differences in resistance to degradation do not result exclusively from lower effective diffusivity per se, but from a combination of lower local diffusivity through presence of strong traps and the fully ferritic microstructure being inherently more resilient than the dual-phase microstructure containing martensite. In other words, there are differences in critical hydrogen concentration between the two microstructures.

4. Conclusions

This study has compared the hydrogen embrittlement susceptibility of ferrite nanoprecipitate to that of conventional ferritic-martensitic advanced high-strength steels (AHSS) of equivalent strength levels via slow strain-rate tests. Hydrogen diffusion coefficients were measured and compared via use of potentiostatic permeation. As these steels are often used with a hot-dipped zinc coating, the Scanning Vibrating Electrode Technique, SVET, was used to quantify the cathodic polarisation of a steel substrate due to galvanic corrosion of a sacrificial zinc coating, and the prospective hydrogen evolution was assessed.

Carried out SVET scans have shown that hydrogen evolution, due to galvanic corrosion, takes place on the steel substrate when the Zn sacrificial coating becomes damaged in 0.1 M NaCl solution. The measured current density at the most strongly cathodic regions was equivalent to that for potentiostatic charging at -1050 mV (SCE) in a 3.5% NaCl + 3 g/L NH_4SCN solution used for both the hydrogen permeation and slow strain-rate tests.

Hydrogen permeation tests have shown that FNP AHSS have lower effective diffusion coefficients, D_{eff} , than FM AHSS of equivalent strength level. At 800 MPa the mean strength levels D_{eff} were 1.68×10^{-7} cm²/s for the FNP800, and 1.87×10^{-7} cm²/s for the FM800. At higher strength levels, 1000 MPa, D_{eff} was 7.45×10^{-8} cm²/s for the FNP1000 and 1.45×10^{-7} cm²/s for the FM1000, respectively. FNP1000 lower D_{eff} values are attributed to the high density of micro-alloyed carbide nanoprecipitates that behave like irreversible hydrogen traps. This was shown in the permeation curves deviations from simulated lattice diffusion curves where the breakthrough time, t_b , was much longer than those for the modelled Fick's equation.

For a given strength level, FNP AHSS were substantially more resistant to hydrogen embrittlement than conventional FM AHSS. The FNP800 and FNP1000 showed embrittlement indices of 32% and 44%, respectively. Meanwhile, FM800 and FM1000 had embrittlement indices of 50% and 76%, respectively, under the same conditions. These differences in susceptibility are attributed to the lower diffusivity found in FNP steels. For higher diffusivity there is increased susceptibility to hydrogen embrittlement for both FNP and FM AHSS.

Author Contributions: J.L.: Conceptualisation, Methodology, Software, Validation, Formal analysis, Investigation, Writing—Original craft, Writing—Review and editing, Visualisation, Project administration; E.S.: Conceptualisation, Resources, Writing—Review and editing, Supervision, Project administration, Funding acquisition; N.M.: Conceptualisation, Methodology, Writing—Review and editing, Supervision; D.F.-G.: Conceptualisation, Methodology, Resources, Writing—Original draft, Writing—Review and editing, Visualisation, Supervision. All authors have read and agreed to the published version of the manuscript.

Funding: This research was funded by M2A from the European Social Fund via the Welsh Government (c80816) and Tata Steel.

Data Availability Statement: The original data presented in the study are openly available in FigShare at DOI: 10.6084/m9.figshare.30305026.

Acknowledgments: The authors would like to acknowledge the assistance provided by the Swansea University AIM Facility, which was funded in part by the EPSRC (EP/M028267/1), the European Regional Development Fund through the Welsh Government (80708), and the Ser Solar project via the Welsh Government. This paper is based on the published thesis: Lelliott, J.A. “Hydrogen Embrittlement of Automotive Ultra-High-Strength Steels: Mechanism and Minimisation.”, Swansea University, Swansea, UK, December 2021.

Conflicts of Interest: Authors James Lelliott and Douglas Figueroa-Gordon were employed by the company Tata Steel UK. At the time the research was conducted James Lelliott was affiliated with Swansea University. The remaining authors declare that the research was conducted in the absence of any commercial or financial relationships that could be construed as a potential conflict of interest.

References

1. Lelliott, J.A. Hydrogen Embrittlement of Automotive Ultra-High-Strength Steels: Mechanism and Minimisation. Doctoral Thesis, Swansea University, Swansea, UK, 2021. [\[CrossRef\]](#)
2. Kuziak, R.; Kawalla, R.; Waengler, S. Advanced high strength steels for automotive industry. *Arch. Civ. Mech. Eng.* **2008**, *8*, 103–117. [\[CrossRef\]](#)
3. Broek, C.T. FutureSteelVehicle: Leading edge innovation for steel body structures. *Ironmak. Steelmak.* **2013**, *39*, 477–492. [\[CrossRef\]](#)
4. European Union. Regulation (EU) No 333/2014 of the European Parliament and of the Council of 11 March 2014 Amending Regulation (EC) No 443/2009 to Define the Modalities for Reaching the 2020 Target to Reduce CO₂ Emissions from New Passenger Cars. *Off. J. Eur. Union* **2014**, *103*, 15–21. Available online: <https://eur-lex.europa.eu/eli/reg/2014/333/oj/eng> (accessed on 29 January 2024).
5. Tamarelli, C.M. *AHSS 101: The Evolving Use of Advanced High Strength Steels for Automotive Applications*; Steel Market Development Institute: Detroit, MI, USA, 2011.
6. Higginson, R.L.; Sellars, C.M. *Worked Examples in Quantitative Metallography*; Maney Pub: Leeds, UK, 2003.
7. Kumar, A.; Singh, S.B.; Ray, K.K. Influence of bainite/martensite-content on the tensile properties of low carbon dual-phase steels. *Mater. Sci. Eng. A* **2008**, *474*, 270–282. [\[CrossRef\]](#)
8. Xu, S.; Cao, R.; Gao, J.; Zhang, Y.; Zhao, H.; Wang, S.; Huang, Y.; Wu, G.; Wu, H.; Zhang, C.; et al. Effect of Cr on the phase transformation and interphase nanoprecipitation behaviours of high-strength microalloyed steels. *Mater. Charact.* **2024**, *207*, 113504. [\[CrossRef\]](#)
9. Funakawa, Y.; Shiozaki, T.; Tomita, K.; Yamamoto, T.; Maeda, E. Development of High Strength Hot-rolled Sheet Steel Consisting of Ferrite and Nanometer-sized Carbides. *ISIJ Int.* **2004**, *44*, 1945–1951. [\[CrossRef\]](#)
10. Yang, P.R.; Cai, M.H.; Wu, C.F.; Su, J.H.; Guo, X.P. Strain-rate dependent hot deformation behavior and mechanism of interphase-precipitated Ti-Mo-xNb steels: Physical modeling and characterization. *Mater. Sci. Eng. A* **2018**, *729*, 230–240. [\[CrossRef\]](#)

11. Zhang, Y.; Miyamoto, G.; Furuhashi, T. Enhanced hardening by multiple microalloying in low carbon ferritic steels with interphase precipitation. *Scr. Mater.* **2022**, *212*, 114558. [CrossRef]
12. Katundi, D.; Tosun-Bayraktar, A.; Bayraktar, E.; Toueix, D. Corrosion behaviour of the welded steel sheets used in automotive industry. *J. Achiev. Mater. Manuf. Eng.* **2010**, *38*, 146–153. Available online: www.journalamme.org (accessed on 29 January 2024).
13. Chalaftris, G.; Robinson, M.J. Hydrogen re-embrittlement of high strength steel by corrosion of cadmium and aluminium based sacrificial coatings. *Corros. Eng. Sci. Technol.* **2005**, *40*, 28–32. [CrossRef]
14. Bockris, J.; McBreen, J.; Nanis, L. The Hydrogen Evolution Kinetics and Hydrogen Entry into α -Iron. *J. Electrochem. Soc.* **1965**, *112*, 1025–1031. [CrossRef]
15. Williams, G.; McMurray, H.N. Localized corrosion of magnesium in chloride-containing electrolyte studied by a scanning vibrating electrode technique. *J. Electrochem. Soc.* **2008**, *155*, C340–C349. [CrossRef]
16. McMurray, H.N.; Williams, D.; Worsley, D.A. Artifacts Induced by Large-Amplitude Probe Vibrations in Localized Corrosion Measured by SVET. *J. Electrochem. Soc.* **2003**, *150*, 12–567. [CrossRef]
17. Bhadeshia, H.K.D.H. Prevention of Hydrogen Embrittlement in Steels. *ISIJ Int.* **2016**, *56*, 24–36. [CrossRef]
18. Beachem, C.D. A new model for hydrogen-assisted cracking (hydrogen “embrittlement”). *Metall. Trans.* **1972**, *3*, 441–455. [CrossRef]
19. Robertson, I.M.; Sofronis, P.; Nagao, A.; Martin, M.L.; Wang, S.; Gross, D.W.; Nygren, K.E. Hydrogen Embrittlement Understood. *Metall. Mater. Trans. B* **2015**, *46*, 1085–1103. [CrossRef]
20. Johnson, W.H. On some remarkable changes produced in iron and steel by the action of hydrogen and acids. *Nature* **1875**, *11*, 393. [CrossRef]
21. Devanathan, M.A.V.; Stachurski, Z. The adsorption and diffusion of electrolytic hydrogen in palladium. *Proc. R. Soc. Lond. A* **1962**, *270*, 90–102.
22. Meister, S. *Grain and Particle Analysis with Line Intersection Method*; Mathworks: Natick, MA, USA, 2012. Available online: <https://uk.mathworks.com/matlabcentral/fileexchange/35203-grain-and-particle-analysis-with-line-intersection-method> (accessed on 18 April 2020).
23. Frank, E.; Hall, M.A.; Witten, I.H. *The WEKA Workbench, Online Appendix for “Data Mining: Practical Machine Learning Tools and Techniques”*, 4th ed.; Morgan Kaufman: Burlington, MA, USA, 2009.
24. Saai, A.; Hopperstad, O.S.; Granbom, Y.; Lademo, O.G. Influence of Volume Fraction and Distribution of Martensite Phase on the Strain Localization in Dual Phase Steels. *Procedia Mater. Sci.* **2014**, *3*, 900–905. [CrossRef]
25. Bergström, Y.; Granbom, Y.; Sterkenburg, D. A Dislocation-Based Theory for the Deformation Hardening Behavior of DP Steels: Impact of Martensite Content and Ferrite Grain Size. *J. Metall.* **2010**, *2010*, 647198. [CrossRef]
26. Sullivan, J.; Cooze, N.; Gallagher, C.; Lewis, T.; Prosek, T.; Thierry, D. In-situ monitoring of corrosion mechanisms and phosphate inhibitor surface deposition during corrosion of Zinc Magnesium Aluminium (ZMA) alloys using novel time-lapse microscopy. *Faraday Discuss.* **2015**, *180*, 361–379. Available online: <http://rsc.li/fd-upcoming-meetings> (accessed on 14 July 2020). [CrossRef] [PubMed]
27. BS EN ISO 17081:2014; Method of Measurement of Hydrogen Permeation and Determination of Hydrogen Uptake and Transport in Metals by an Electrochemical Technique. B.S. Institute: London, UK, 2014.
28. Henthorne, M. The slow strain rate stress corrosion cracking test—A 50 year retrospective. *Corrosion* **2016**, *72*, 1488–1518. [CrossRef]
29. BS EN ISO 6892-1:2016; Metallic Materials. Tensile Testing. Method of Test at Room Temperature. B.S. Institute: London, UK, 2016. Available online: <https://bsol.bsigroup.com/Bibliographic/BibliographicInfoData/00000000030268532> (accessed on 18 April 2020).
30. Gong, K.; Sun, D.; Liu, X.; Li, J.; Wu, M.; Hu, M. Effects of hydrogen and strain rate on stress corrosion cracking mechanism of high strength pipeline steel. *Mater. Today Commun.* **2025**, *44*, 112172. [CrossRef]
31. Hojo, T.; Kikuchi, R.; Waki, H.; Nishimura, F.; Ukai, Y.; Akiyama, E. Effect of strain rate on the hydrogen embrittlement property of ultra high-strength low alloy TRIP-aided steel. *ISIJ Int.* **2018**, *58*, 751–759. [CrossRef]
32. Momotani, Y.; Shibata, A.; Terada, D.; Tsuji, N. Effect of strain rate on hydrogen embrittlement in low-carbon martensitic steel. *Int. J. Hydrogen Energy* **2017**, *42*, 3371–3379. [CrossRef]
33. Momotani, Y.; Shibata, A.; Yonemura, T.; Bai, Y.; Tsuji, N. Effect of initial dislocation density on hydrogen accumulation behavior in martensitic steel. *Scr. Mater.* **2020**, *178*, 318–323. [CrossRef]
34. Toribio, J.; Vergara, D.; Lorenzo, M. Influence of loading rate on the hydrogen-assisted micro-damage in bluntly notched samples of pearlitic steel. *Metals* **2016**, *6*, 11. [CrossRef]
35. Xing, Y.; Yang, Z.; Zhao, Q.; Zhang, L. Hydrogen Permeation Behavior of X80 Steel under Constant and Slow Strain Rate Tension Stress. *J. Mater. Eng. Perform.* **2025**, *34*, 19154–19165. [CrossRef]
36. Figueroa, D.; Robinson, M.J. Hydrogen transport and embrittlement in 300 M and AerMet100 ultra high strength steels. *Corros. Sci.* **2010**, *52*, 1593–1602. [CrossRef]

37. Robinson, M.J.; Sharp, R.M. The Effect of Post-Exposure Heat Treatment on the Hydrogen Embrittlement of High Carbon Steel. *Corrosion* **1985**, *41*, 582–586. [\[CrossRef\]](#)
38. Akiyama, E.; Li, S. Electrochemical hydrogen permeation tests under galvanostatic hydrogen charging conditions conventionally used for hydrogen embrittlement study. *Corros. Rev.* **2016**, *34*, 103–112. [\[CrossRef\]](#)
39. Lan, L.; Kong, X.; Hu, Z.; Qiu, C.; Zhao, D.; Du, L. Hydrogen permeation behavior in relation to microstructural evolution of low carbon bainitic steel weldments. *Corros. Sci.* **2016**, *112*, 180–193. [\[CrossRef\]](#)
40. Van den Eeckhout, E.; Depover, T.; Verbeken, K. The Effect of Microstructural Characteristics on the Hydrogen Permeation Transient in Quenched and Tempered Martensitic Alloys. *Metals* **2018**, *8*, 779. [\[CrossRef\]](#)
41. Dadfarnia, M.; Sofronis, P.; Neeraj, T. Hydrogen interaction with multiple traps: Can it be used to mitigate embrittlement? *Int. J. Hydrogen Energy* **2011**, *36*, 10141–10148. [\[CrossRef\]](#)
42. Iino, M. Trapping of hydrogen by sulfur-associated defects in steel. *Metall. Trans. A* **1985**, *16*, 401–409. [\[CrossRef\]](#)
43. Depover, T.; Verbeken, K. The effect of TiC on the hydrogen induced ductility loss and trapping behavior of Fe-C-Ti alloys. *Corros. Sci.* **2016**, *112*, 308–326. [\[CrossRef\]](#)
44. Depover, T.; Monbaliu, O.; Wallaert, E.; Verbeken, K. Effect of Ti, Mo and Cr based precipitates on the hydrogen trapping and embrittlement of Fe-C-X Q&T alloys. *Int. J. Hydrogen Energy* **2015**, *40*, 16977–16984. [\[CrossRef\]](#)
45. Depover, T.; Laureys, A.; Escobar, D.P.; Van den Eeckhout, E.; Wallaert, E.; Verbeken, K. Understanding the Interaction between a Steel Microstructure and Hydrogen. *Materials* **2018**, *11*, 698. [\[CrossRef\]](#) [\[PubMed\]](#)
46. Lee, J.; Lee, T.; Kwon, Y.J.; Mun, D.-J.; Yoo, J.-Y.; Lee, C.S. Effects of vanadium carbides on hydrogen embrittlement of tempered martensitic steel. *Met. Mater. Int.* **2016**, *22*, 364–372. [\[CrossRef\]](#)
47. Takahashi, J.; Kawakami, K.; Kobayashi, Y.; Tarui, T. The first direct observation of hydrogen trapping sites in TiC precipitation-hardening steel through atom probe tomography. *Scr. Mater.* **2010**, *63*, 261–264. [\[CrossRef\]](#)
48. Chen, Y.S.; Haley, D.; Gerstl, S.S.; London, A.J.; Sweeney, F.; Wepf, R.A.; Rainforth, W.M.; Bagot, P.A.; Moody, M.P. Direct observation of individual hydrogen atoms at trapping sites in a ferritic steel. *Science* **2017**, *355*, 1196–1199. [\[CrossRef\]](#)
49. Martínez-Madrid, M.; Chan, S.L.I.; Charles, J.A.; López L, J.A.; Castaño, V. Effect of grain size and second phase particles on the hydrogen occlusivity of iron and steels. *Mater. Res. Innov.* **2000**, *3*, 263–270. [\[CrossRef\]](#)
50. Maki, T. 2—Morphology and substructure of martensite in steels. In *Phase Transformations in Steels*; Pereloma, E., Edmonds, D.V., Eds.; Woodhead Publishing: Sawston, UK, 2012; pp. 34–58. [\[CrossRef\]](#)
51. Takai, K.; Seki, J.; Homma, Y. Observation of Trapping Sites of Hydrogen and Deuterium in High-Strength Steels by Using Secondary Ion Mass Spectrometry. *Mater. Trans. JIM* **1995**, *36*, 1134–1139. [\[CrossRef\]](#)
52. Hagi, H. Diffusion Coefficient of Hydrogen in Iron without Trapping by Dislocations and Impurities, Materials Transactions. *JIM* **1994**, *35*, 112–117. [\[CrossRef\]](#)
53. Hagi, H.; Hayashi, Y. Effect of Dislocation Trapping on Hydrogen and Deuterium Diffusion in Iron. *Trans. Jpn. Inst. Met.* **1987**, *28*, 368–374. [\[CrossRef\]](#)
54. Koyama, M.; Tasan, C.C.; Akiyama, E.; Tsuzaki, K.; Raabe, D. Hydrogen-assisted decohesion and localized plasticity in dual-phase steel. *Acta Mater.* **2014**, *70*, 174–187. [\[CrossRef\]](#)
55. Takashima, K.; Nishimura, T.; Yokoyama, K.; Funakawa, Y. Role of Interface between Ferrite and Martensite in Hydrogen Embrittlement Behavior of Ultra-high Strength Dual-phase Steel Sheets. *ISIJ Int.* **2019**, *59*, 1676–1682. [\[CrossRef\]](#)
56. Zhang, S.; Liu, S.; Wan, J.; Liu, W. Effect of Nb-Ti multi-microalloying on the hydrogen trapping efficiency and hydrogen embrittlement susceptibility of hot-stamped boron steel. *Mater. Sci. Eng. A* **2020**, *772*, 138788. [\[CrossRef\]](#)
57. Laureys, A.; Pinson, M.; Claeys, L.; De Seranno, T.; Depover, T.; Verbeken, K. Initiation of hydrogen induced cracks at secondary phase particles. *Frat. Integrata Strutt.* **2020**, *14*, 113–127. [\[CrossRef\]](#)
58. Takahashi, J.; Kawakami, K.; Kobayashi, Y. Origin of hydrogen trapping site in vanadium carbide precipitation strengthening steel. *Acta Mater.* **2018**, *153*, 193–204. [\[CrossRef\]](#)
59. Rodoni, E.; Verbeken, K.; Depover, T.; Iannuzzi, M. Effect of microstructure on the hydrogen embrittlement, diffusion, and uptake of dual-phase low alloy steels with varying ferrite-martensite ratios. *Int. J. Hydrogen Energy* **2024**, *50*, 53–65. [\[CrossRef\]](#)

Disclaimer/Publisher’s Note: The statements, opinions and data contained in all publications are solely those of the individual author(s) and contributor(s) and not of MDPI and/or the editor(s). MDPI and/or the editor(s) disclaim responsibility for any injury to people or property resulting from any ideas, methods, instructions or products referred to in the content.